APPLIED SCIENCES AND ENGINEERING

A sensor-actuator–coupled gustatory interface chemically connecting virtual and real environments for remote tasting

Shulin Chen[1]†, Yizhen Jia[1]†, Bowen Duan[2]†, Tzu-Li Liu[1], Qi Wang[1], Xiao Xiao[3,4], Prasad Nithianandam[1], Xi Tian[5], Chunyu Yang[1], Changsheng Wu[3,4,6,7], Zhaoqian Xie[2,8]*, Jinghua Li[1,9]*

Recent advancements in virtual reality (VR) and augmented reality (AR) have strengthened the bridge between virtual and real worlds via human-machine interfaces. Despite extensive research into biophysical signals, gustation, a fundamental component of the five senses, has experienced limited progress. This work reports a bio-integrated gustatory interface, "e-Taste," to address the underrepresented chemical dimension in current VR/AR technologies. This system facilitates remote perception and replication of taste sensations through the coupling of physically separated sensors and actuators with wireless communication modules. By using chemicals representing five basic tastes, systematic codesign of key functional components yields reliable performance including tunability, versatility, safety, and mechanical robustness. Field testing involving human subjects focusing on user perception confirms its proficiency in digitally simulating a range of taste intensities and combinations. Overall, this investigation pioneers a chemical dimension in AR/VR technology, paving the way for users to transcend visual and auditory virtual engagements by integrating the taste sensation into virtual environment for enhanced digital experiences.

INTRODUCTION

Human-machine interfaces (HMIs) have gained substantial attention due to their potential applications in virtual reality (VR) and augmented reality (AR) (*1*–*3*). By blending interactive virtual environments with the real world, these systems integrate signal inputs and actuations to enhance user experiences. Recent years have witnessed the emergence of advanced HMIs in various fields such as immersive gaming, prosthesis control, teleoperation, global collaboration, biomedical research, and physical therapy (*4*–*11*). Despite the great success, most existing HMIs focus on biophysical inputs and outputs such as electrophysiological, haptic, audio, and visual signals (*7*, *12*–*21*). In contrast, HMIs involving chemical cues remain highly unexplored due to challenges in capturing and simulating these signals and the limited pioneering research on sensory interactions.

Gustation, an essential component of the human perceptual system, plays a key role in the overall sensory experience and flavor perception. However, the integration of gustation is currently limited or missing in most AR/VR experiences. While pioneering works have reported on the digital generation of taste sensation and successfully demonstrated promising results (*22*), the field of gustatory interfaces requires further exploration in several areas, including quantitative taste generation, programmable mixing, coupled sensor-actuator operation, bio-integrated formats, and validation through field testing (note S1 and table S1). Specifically, challenges pertain to the following aspects: (i) There are no standardized methodologies for digitally generating the taste sensation yet. Direct electrical and thermal tongue stimulation limits the simulation of tastes to only a few ones. Similar to gustation, researchers have also attempted to simulate smell through electrical stimulation of the inner nose but only achieved limited success thus far (*23*). The alternative strategy of chemical release from media, while offering more flavor diversity, also encounters difficulties in achieving rapid, reliable, and universal implementation across platforms (*22*, *24*). (ii) As the taste bud distribution on the tongue is not uniform and varies across different regions (*25*), it is necessary to develop interfaces that can accurately target specific areas/taste receptors for understanding gustatory pathways in biomedical research. (iii) Previous studies have focused on gustatory sensory (*26*–*28*) or taste augment systems (*22*, *24*) in isolation. Their integration and coupling, while could be useful to connect users with the remote world, remain underexplored. (iv) The bulky and rigid structures and obtrusive implementation of existing gustatory interfaces (*7*, *22*, *29*) hinder their wearability, mobility, and user comfortness.

As a result, existing gustatory interfaces fall far behind visual and auditory-based VR/AR counterparts. It is necessary to establish a framework that enables precise and digitally controlled gustatory sensation. This work reports a bio-integrated gustatory interface that chemically connects physically distant spaces through an Internet of Things (IoT) strategy and enables remote tasting. By combining materials, devices, software, and hardware, the system offers a unified chemical platform capable of facilitating digital conduits that connect humans across physically distant real spaces. The primary component is a quantitative, localized, customizable, and easily controlled

[1]Department of Materials Science and Engineering, The Ohio State University, Columbus, OH 43210, USA. [2]Department of Engineering Mechanics, Dalian University of Technology, Dalian 116024, China. [3]Institute for Health Innovation and Technology, National University of Singapore, Singapore 117599, Singapore. [4]Department of Electrical and Computer Engineering, National University of Singapore, Singapore 117583, Singapore. [5]Tsinghua Shenzhen International Graduate School, Tsinghua University, Nanshan, Shenzhen 518071, China. [6]Department of Materials Science and Engineering, National University of Singapore, Singapore 117575, Singapore. [7]The N.1 Institute for Health, National University of Singapore, Singapore 117456, Singapore. [8]State Key Laboratory of Structural Analysis, Optimization and CAE Software for Industrial Equipment, Dalian University of Technology, Dalian, 116024, China. [9]Chronic Brain Injury Program, The Ohio State University, Columbus, OH 43210, USA.
*Corresponding author. Email: li.11017@osu.edu (J.L.); zxie@dlut.edu.cn (Z.X.)
†These authors contributed equally to this work.

liquid delivery system using electromagnetic (EM) actuation. TA flexible design for the gustatory interface allows for better integration with the human body, enabling effortless implementation compared to conventional bulky alternatives. This is particularly advantageous when users are engaged in complex tasks, such as next-generation VR/AR applications or biomedical research (Fig. 1A). The gustatory interface reported here addresses limitations in unobtrusive implementation, spatial targeting capability, mixing function, and sensor-actuator coupling, in comparison to existing gustatory interfaces. Table S1 shows a detailed comparison, along with relevant references. Figure 1B illustrates the working principles and logic behind key steps in operating the sensor-actuator–coupled system, including taste information capture and encoding, signal decoding for waveform control, tastant diffusion from hydrogels for concentration regulation, and taste generation to elicit user perception in accordance with Stevens' power law (more details provided in the following sections). Coupled via a data processing module, the key demonstrator, "e-Taste," comprises two key functional components: (i) a sensing

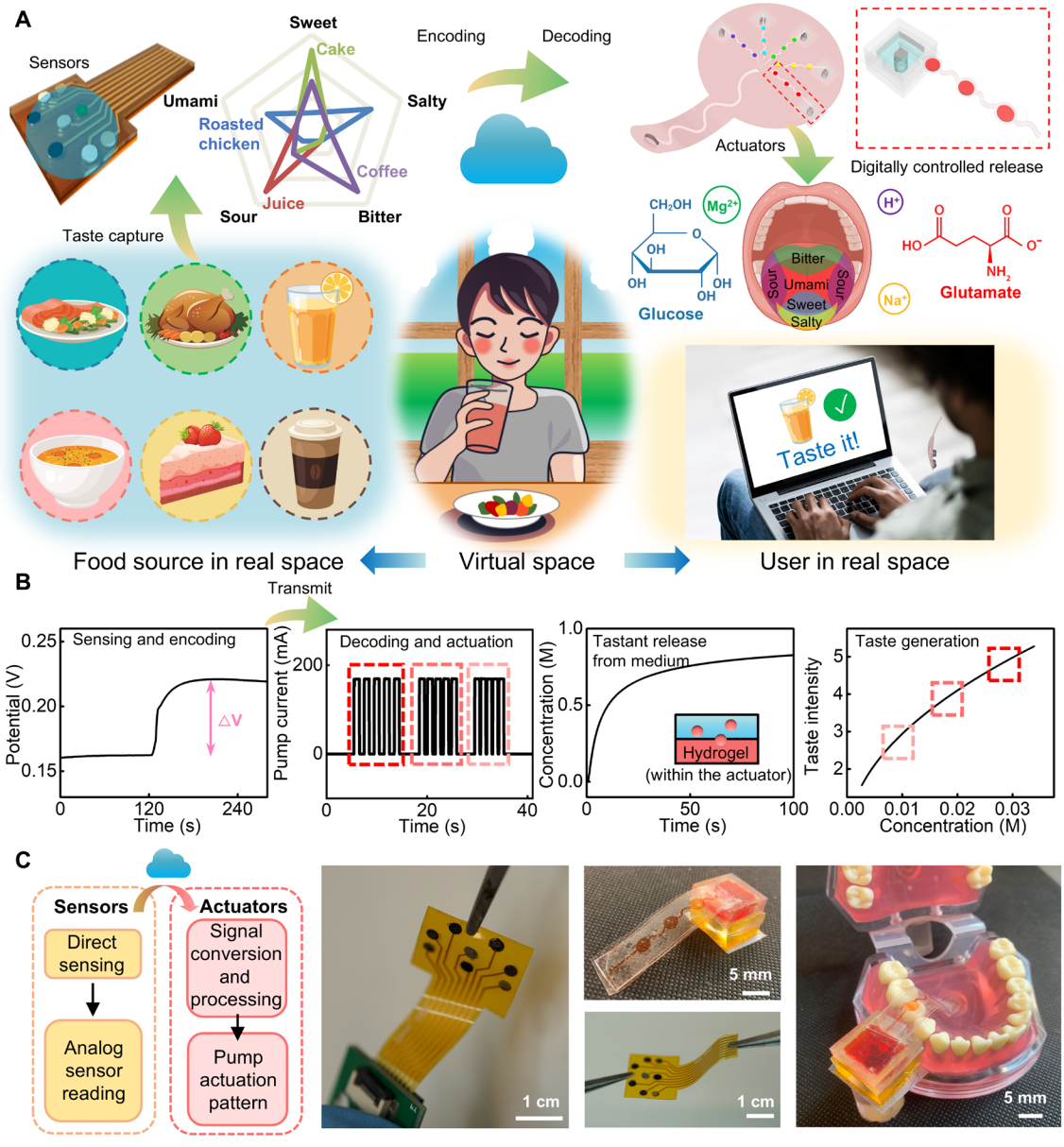

Fig. 1. Overview of the e-Taste system, including the working principles, data transmission scheme, and key functional units. (**A**) Schematic illustration of the operational principle of the reported gustatory interface, e-Taste. It features an electrochemical sensing platform for taste information capture, a wireless data transmission protocol for remote instruction and control, and an EM actuation system for taste replication by using edible chemicals representing the five basic taste sensations. The e-Taste can bridge real and virtual spaces or connect disparate real spaces across long distances (images used under license from Adobe Stock). (**B**) Working principles and logic behind key steps in operating the sensor-actuator–coupled system, including a sensing curve, control signal for actuation, diffusion model for tastant release from hydrogel media, and Stevens' power law for taste perception. (**C**) Flow chart of the data processing module, together with photographs of a multichannel sensor patch and an EM actuator with colored liquid inside, mounted onto a dental cast.

platform that captures taste chemicals in a target system, providing information for remote control and instruction and (ii) an EM actuation system that delivers edible taste chemicals through a microfluidic interface (Fig. 1C and fig. S1). Specifically, the actuation component focuses on a class of hydrogel-based, electro-responsive interfaces for digitally controlled chemical release. The study uses the following chemicals to represent the five basic tastes: glucose, sweet; citric acid, sour; NaCl, salty; $MgCl_2$, bitter; and glutamate, umami (*24*, *30*, *31*). Systematic studies establish design principles and determine the performance in sensing, communication, actuation, and delivery. Field testing evaluates how human subjects perceive and engage with remote tasting experiences facilitated by e-Taste during practical applications such as digital food sharing and immersive games. Beyond the scope of this study, incorporating additional taste chemicals and sensing/actuation modalities can generalize the implementation of this concept and device model. In addition, the evaluation of user safety explored in this work aims to contribute to the formulation of safety standards to govern this emerging field of gustatory interfaces for the next generation HMIs. The results here pave the way for the next generation VR/AR technology that allows users to not only see and hear virtual environments but also taste them through interaction with digital content.

RESULTS

Design, working principle, and characterization of EM actuators

The actuator uses an EM minipump to deliver concentration-controlled tastant solutions into the oral cavity. Figure 2A shows schematic illustration of the EM actuator consisting of a microfluidic channel and a minipump that includes a polydimethylsiloxane (PDMS) liquid chamber, NdFeB permanent magnets, and a coil placed perpendicular to the magnet (*32*). The design details and fabrication process of the EM actuator are in figs. S2 and S3. The outlet of the liquid chamber connects to the refillable microfluidic channel embedded with tastant-infused gels (fig. S4). The equivalent circuit of the system appears on the right. A bipolar junction transistor (BJT) serves as an "on/off" switch through a pulse width modulation (PWM) base current received from an ESP32 chip microcontroller. The actuation system uses an NPN-type transistor (2N2222), within which electrons serve as the majority charge carriers. As electrons have higher mobility compared to holes, this selection allows the BJT to respond quickly to high frequency voltage signals for robust and reliable operation. This switch leads to the generation of an alternating magnetic field across the coil, subsequently driving the vibration of the magnet (note S2). The periodic deformation of the capping membrane triggered by the vibration actuates the pumping of the liquid into the microfluidic channel. Designing the inlet to be much smaller than the outlet creates a pressure gradient and ensures the unidirectional flow upon the movement of the diaphragm. Liquid flows through the channel during the "on" state and stops temporarily during the "off" state, allowing interaction with the hydrogels with tastants. Adjusting the duty cycle controls the time that the liquid takes to traverse the microfluidic channel, thereby regulating the concentrations of taste chemicals in the resulting solution. A larger interval time (t) between pulses corresponds to a longer period of the liquid contacting the gels, increasing the resulting concentration of tastants in the delivered solutions. The interaction between the liquid and tastant-infused gels is related to factors such as molecular size, ionic charge, and the nature of the hydrogel matrix. These factors collectively determine the diffusion rates of tastants, which are critical for accurately replicating taste profiles. Detailed explanation and characterization of this diffusion process are in figs. S5 and S6 and note S3. Specially, fig. S5 (A to C) demonstrates the fabrication process of the hydrogel including mixing, ultraviolet (UV) curing, and crosslinking. The formation of a crosslinked network encapsulates the tastant, making it the only soluble component.

As the current flowing through the coil increases from 0 to 180 mA, the diaphragm experiences a corresponding increase in deformation (Fig. 2B) (up to 2 mm along the vertical direction). Figure 2C shows a series of photographs demonstrating the pumping process. Operating at a current of 180 mA, the system facilitates delivery of liquids through the channel within 10 s. For each actuation, using a consistent number of pumping cycles and varying the time intervals (0, 0.2, 0.4, 0.6, 0.8, and 1.0 s) between each cycle modulate the concentrations of taste chemicals in liquids with a consistent volume. The direct correlation between current and the deformation of the diaphragm results in a larger volume of delivered liquid as the current increases. Figure 2 (D and E) demonstrate the capability of the system in controlling the pumping process at multiple dimensions by varying the actuation parameters. Using Fig. 2D (top) as a reference (amplitude: 3.3 V, frequency: 0.5 Hz, duty cycle: 50%), Fig. 2D (bottom) shows the modulation of frequency (0.67 Hz), while Fig. 2E shows the modulation of amplitude (top, 2.0 V) and duty cycle (bottom, 35%) of the PWM current. Figure 2F displays the total volume of liquid pumped out over a span of 10 s at a direct current ranging from 20 to 260 mA, yielding a transported volume between 0 and 58 μl. This volume is perceptible to the tongue, as a single drop of water typically measures around 50 μl (*33*–*35*). Expanding these designs to various length scales can enable the dispensing of the required amount of liquids as needed.

Notably, the coil temperature rises during operation over time under continuous operation with a constant current applied (Fig. 2G). This may lead to concerns about instability of the system during the actuation, together with user acceptance and/or safety issues. As a result, the data shown here aim to characterize the thermal behavior, capability, and limits of the system. In real practice, pulsed currents can allow for cooling between cycles to mitigate these risks (details in the following section and Fig. 3). Balancing temperature and volume considerations, the study uses a current of 180 mA, which yields approximately 40 μl of liquid and maintains a moderate temperature, 42°C, after running for 20 s. Figure 2 (H to L) demonstrates the variations in concentrations of five taste-related chemicals (H^+, Mg^{2+}, Na^+, glucose, and glutamate) in the resulting solutions in response to different time intervals. By executing 10 1-s pulses, the increase in interval time from 0 to 1.0 s results in the following concentration ranges: H^+ varies from 0.195 to 8.738 mM, Mg^{2+} from 2.670 to 6.558 mM, Na^+ from 0.108 to 0.212 M, glucose from 3.27 to 54.81 mM, and glutamate from 0.825 to 1.362 mM. These concentration ranges allow for a distinguishable representation of tastes, enabling the recreation of many food types (*36*–*41*). Refining the coupling between the hydrogel and actuation protocols, in principle, can further broaden the concentration range based on the specific requirements of target applications. For wireless operation, a LiPo battery (3.7 V, 100 mAh) sustains more than 1850 actuation cycles of 1-s pulses for repetitive use (fig. S7). Figure S8 presents additional results of the response time, detailing the duration from EM actuation to liquid release from the chamber, along with supporting

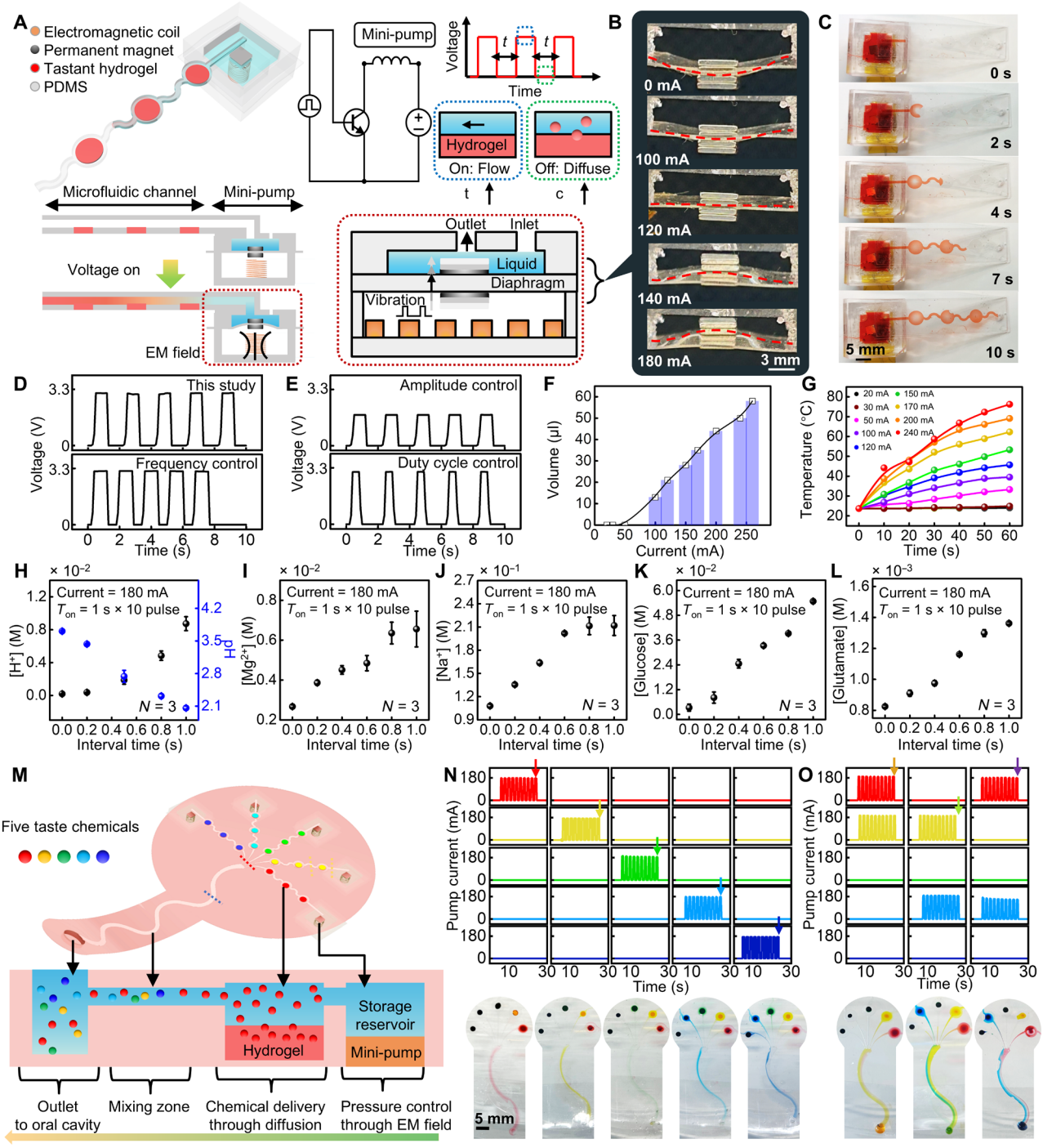

Fig. 2. Characterization of the gustatory interface including the EM actuators and the microfluidics. (**A**) Schematic illustration of the EM minipump including a PDMS liquid chamber, NdFeB permanent magnets, a coil, and a microfluidic channel, together with the working principle of the actuator. (**B**) Photographs showing the deformation of the thin PDMS film with magnets according to an increased current in the coil. (**C**) Sequential photographs showing the delivery of liquid during a 10-s pumping process. (**D** and **E**) Controlled pumping current depicted with variable actuation parameters showing the tunability of the actuation process across a broad spectrum of amplitude, frequency, and duty cycle. (**F**) Liquid volume delivered from the channel following a 10-s pumping at various current amplitudes. (**G**) Effect of current amplitude on the temperature rise of the coil over a 60-s period of constant current. (**H** to **L**) Concentration changes of five basic taste-related chemicals (H^+, Mg^{2+}, Na^+, glucose, and glutamate) in response to different time intervals during actuation. (**M**) Schematic illustration of an integrated multi-channel system consists of a set of EM pumps, sample reservoirs, interconnecting channels, and a mixing zone. (**N** and **O**) Demonstration with water soluble dyes loaded in different channels showing the capability of the microfluidics in liquid mixing. The individual channels can work either separately or concurrently.

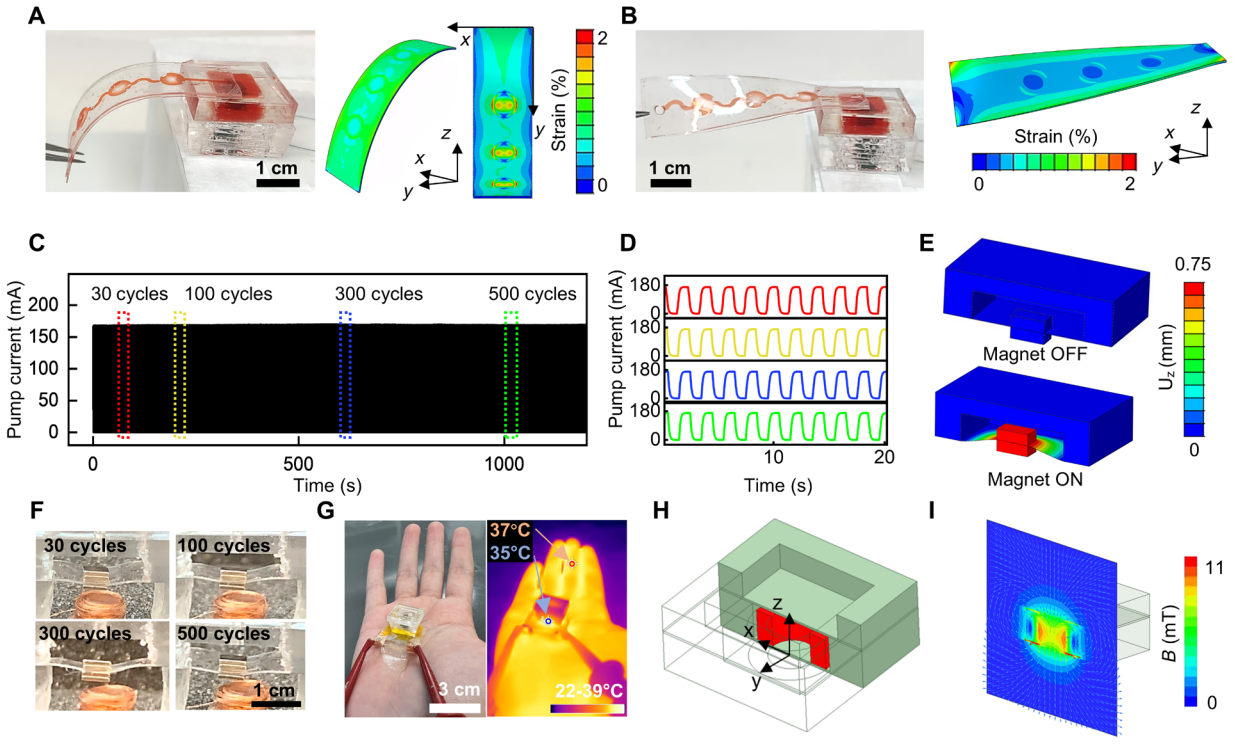

Fig. 3. Stability and safety evaluation of the EM actuation system. (**A** and **B**) FEA simulations and the corresponding photographs of the EM actuator under conditions of bending and twisting. (**C**) A record of pumping current for continuous operation over 500 cycles (pulse width: 1 s, 50% duty cycle), along with (**D**) zoomed-in curves after 30, 100, 300, and 500 cycles respectively, (**E**) simulations of the pump with current on and off, and (**F**) corresponding photographs after repetitive actuation cycles. (**G**) Optical image and IR image of the actuator on a hand after 100 actuation cycles. (**H**) Model used in FEA for calculating the magnetic field distribution around the coil. (**I**) Magnetic flux density distributions in *z*-*x* plane.

photographs and a summarized table S2. The results suggest a relatively high release speed of the system.

Design of flexible microfluidics for liquid routing, mixing, and management

Scaling up the system to include multiple tastant channels allows for the generation of complex gustation with digitally tunable compositions. This study uses a microfluidic interface to enable the mixing and subsequent delivery. Figure 2M shows a five-channel system consisting of a set of sample reservoirs, interconnecting channels, and a mixing zone. Detailed dimensions appear in fig. S2. Upon the actuation, liquids from each channel enter the mixing zone with a winding channel structure for effective blending (*42*). The resultant liquid then proceeds to the oral cavity through the outlet. In this design, the microfluidic outlet interfaces with the oral cavity, while the EM minipumps can be attached to the dry area of the human body. This configuration minimizes potential risks to users because the electronics remain shielded from exposure to the wet environments. Note that the system does not incorporate a selective release mechanism, as each channel contains only one tastant that can be individually controlled. This design prevents potential interference and allows for programmable mixing of solutions based on the input control.

Figure S9A shows the cross-sectional scanning electron microscope (SEM) images of the individual channel area (yellow dashed box), premixing part (red dashed box), and the mixing zone (blue dashed box). The width of the five channels leading into the premixing region is 100 μm, approximately 30 times narrower than the 3 mm width of the mixing channel. This configuration minimizes sources of backpressure and fluidic drag, thus facilitating the smooth flow and efficient mixing (*43*, *44*). Figure S9B presents multiple photographs of the microfluidics under both flat and bent states, indicative of the mechanical flexibility and compliance as a bio-interface. While concentrations can be demonstrated through numerical data, using colored dyes as substitutes allows presenting the mixing process more convincingly through photos. Considering this, Fig. 2 (N and O) illustrates the mixing function of our system in a more intuitive way using multiple samples. Controlling each channel filled with food dyes with distinct colors individually/simultaneously visualizes the programmable operation: Figure 2N (top) shows the voltage profiles used to activate individual actuators. Correspondingly, Fig. 2N (bottom) demonstrates that the color of the liquid within the mixing channel and at the outlet changes in alignment with the activation of the respective actuators. Figure 2O (top) depicts the concurrent voltage profiles that activate two different actuators at the same time. As illustrated in Fig. 2O (bottom), the efficient blending of dyes from dual channels (red + yellow = orange, yellow + blue = green, and red + blue = navy) showcases the capability of the system to concurrently pump and mix fluids.

Stability and safety evaluation of the EM actuation system

Figure 3 presents results showing the resilience and robustness of e-Taste across mechanical, electrical, and thermal dimensions for use as bio-integrated electronics. The photographs and finite element

analysis (FEA) data (Fig. 3, A and B) illustrate the capacity of the system to withstand bending at an angle of approximately 90° (maximum strain of <2%) and twisting at approximately 60° (maximum strain of <2%), along the orientation of the microfluidics. Introducing red ink into the channel indicates deformations do not induce notable fluid displacement within the channel nor compromise the integral connection of the channel to the pump. Figure 3C illustrates the measured current passing through the coil over more than 500 cycles of an actuating PWM (pulse width: 1 s, 50% duty cycle). Zoomed-in views of the current captured at 30, 100, 300, and 500 cycles appear in Fig. 3D, with the corresponding FEA simulations of the pump with current on and off in Fig. 3E. The diaphragm exhibits no plastic deformation throughout 500 actuation cycles (Fig. 3F). These results indicate consistency and robustness during prolonged, repetitive actuation. In addition, fig. S10 illustrates the condition and performance characterizations of the microfluidic channel device before, during, and after exposure to clipping 500 times at the outlet, simulating scenarios where the outlet might be compressed, such as being bitten. These results demonstrate the mechanical stability and sustained functionality of the system under realistic usage conditions.

Figure S11 and Fig. 3G present the evaluation of the thermal safety of the system over prolonged actuation. As shown in fig. S11A, compared to the room temperature, the change in H^+ concentration slightly increases at body temperature due to an increased diffusivity of tastants, with the general trend remaining the same. With pulsed actuation allowing sufficient cooling time between cycles, the temperature of the coil increases only slightly from 24.5° to 28°C after 20 s (equivalent to 10 cycles of square waves), in contrast to the rise to 42°C observed in Fig. 2G with a constant current (fig. S11B). Only after 100 actuation cycles (spanning 200 s)—a duration far exceeding the number of actuation cycles used in this study—does the temperature reach 39°C. These results indicate that pulsed actuation enhances thermal safety for users. Moreover, because of the encapsulation of thermally insulating PDMS chamber, this increase does not notably affect the liquid within the chamber, as shown by the photograph and infrared image in Fig. 3G: The temperature of the liquid chamber stays relatively low (~25°C) after the process. Lastly, the coil chamber is not in direct contact with the oral cavity during the liquid delivery process. These strategies contribute to minimizing risks to users. Figure 3 (H and I) and fig. S12 present a simulation of the EM field during actuation. Compared to the established safe threshold (British Pre-Standard no. 50166-1) for magnetic fields (<300 mT) (*45*), the system exhibits a considerably high safety margin (maximum magnetic flux density < 11 mT) for human exposure. Immersing the microfluidic channel (filled with colored liquid) into water for 30 min does not lead to obvious leakage (fig. S13), suggesting the robustness of the device to operate in liquid environment for delivery with precise spatial targeting.

The wireless electronic tongue for remote acquisition of tastant information

Another essential part of the e-Taste is a multiplexed sensing platform functioning as an "electronic tongue" (*46*) that captures taste chemicals in the target for remote control and instruction. The integration of sensing and actuation in the e-Taste system with wireless signal transmission hardware bridges users with the remote world through digital content. Some envisioned applications in this context include but are not limited to: (i) virtual food adventures and remote tasting experiences for customers during online shopping; (ii) identification, tasting, and analysis of potential food sources in harsh environments; (iii) quality monitoring of "robot chefs" to ensure the safety, freshness, and consistency of the prepared food; (iv) remote healthcare evaluating the taste perception and preferences of participants for real-time feedback and decision making (fig. S14). Figure S15 presents the overall design of the circuits using ESP32 System-on-Chips (SoCs), with detailed circuit diagrams for each part in fig. S16. Table S3 lists all the components used for the circuit. Initially, capturing the concentration data of tastants, the sensor patch connected to the analog-to-digital converters (ADCs) transforms this information into electrical signals. The microcontroller unit (MCU) further processes the signals and wirelessly transmits them to the actuation system. The e-Taste system accommodates two wireless transmission modes: a short-range mode using ESPNOW with a working distance of up to 200 m and a long-range mode with no distance limit via the Internet involving data upload/download using an IoT platform such as Blynk (*47*). When powered by a LiPo battery (3.7 V, 100 mAh), the system sustains data transmission for ~37 min in short-range mode and ~45 min in long-range mode, respectively (fig. S17). This transmitted data serves to control the actuation process.

Aligned with the five tastant chemicals used for the actuators, the study uses the following sensing strategies: (i) enzyme-functionalized sensors for glucose and glutamate (*48*, *49*), which measure the voltage as a result of the Faradaic current generated through redox reactions, and (ii) polyaniline (PANI) or ion selective membrane (ISM) functionalized sensors for H^+, Na^+, and Mg^{2+}, which measure changes in the surface potential at the sensing interface due to the binding of target ions (fig. S18). The design of the sensor patch appears in fig. S19 (*50*). Figure 4 (A to E) shows the calibration curves of the five sensors. The respective sensitivities are: 32.3 mV/decade for H^+, 57.2 mV/decade for Na^+, 26.7 mV/decade for Mg^{2+}, 29.6 mV/mM for glucose, and 11.9 mV/mM for glutamate. Figure S20 shows the high selectivity of the sensors in the presence of the other four nontarget tastants serving as interferents.

Figures S21 and S22 describe the detailed operation logic for remote tasting. The sensors interact with the target to detect the corresponding chemical concentrations. The wireless communication module then transmits the sensor readings in voltage to the actuators. Subsequently, calculations convert the voltage signals back to concentrations based on the pre-established sensor baseline and calibration curve. This concentration information then automatically instructs the operation of the actuator through a control mechanism that categorizes specific concentrations into five distinct intensity levels (very mild, mild, medium, strong, and very strong), each corresponding to different actuation interval times (*51*). This categorization is based on an even distribution across the entire range of concentrations achievable by the actuators. Table S4 and note S4 illustrate an exemplified case using sourness to demonstrate detailed methods for categorization and calculation.

Chemical composition replication experiments using simulated "juice" (Fig. 4F and fig. S23A) and "chicken soup" (Fig. 4G and fig. S23B) (with concentrations from the literature as shown in table S5) serve as illustrative examples to demonstrate this process. The flow chart for each, organized from left to right, presents a sequence of data involved in remote tasting: the actual concentrations of five taste components in these liquids [as reported in previous research (*37*, *52*)], the electrical signals obtained from five sensors, the corresponding cycle times (pumping time + interval time) for actuation

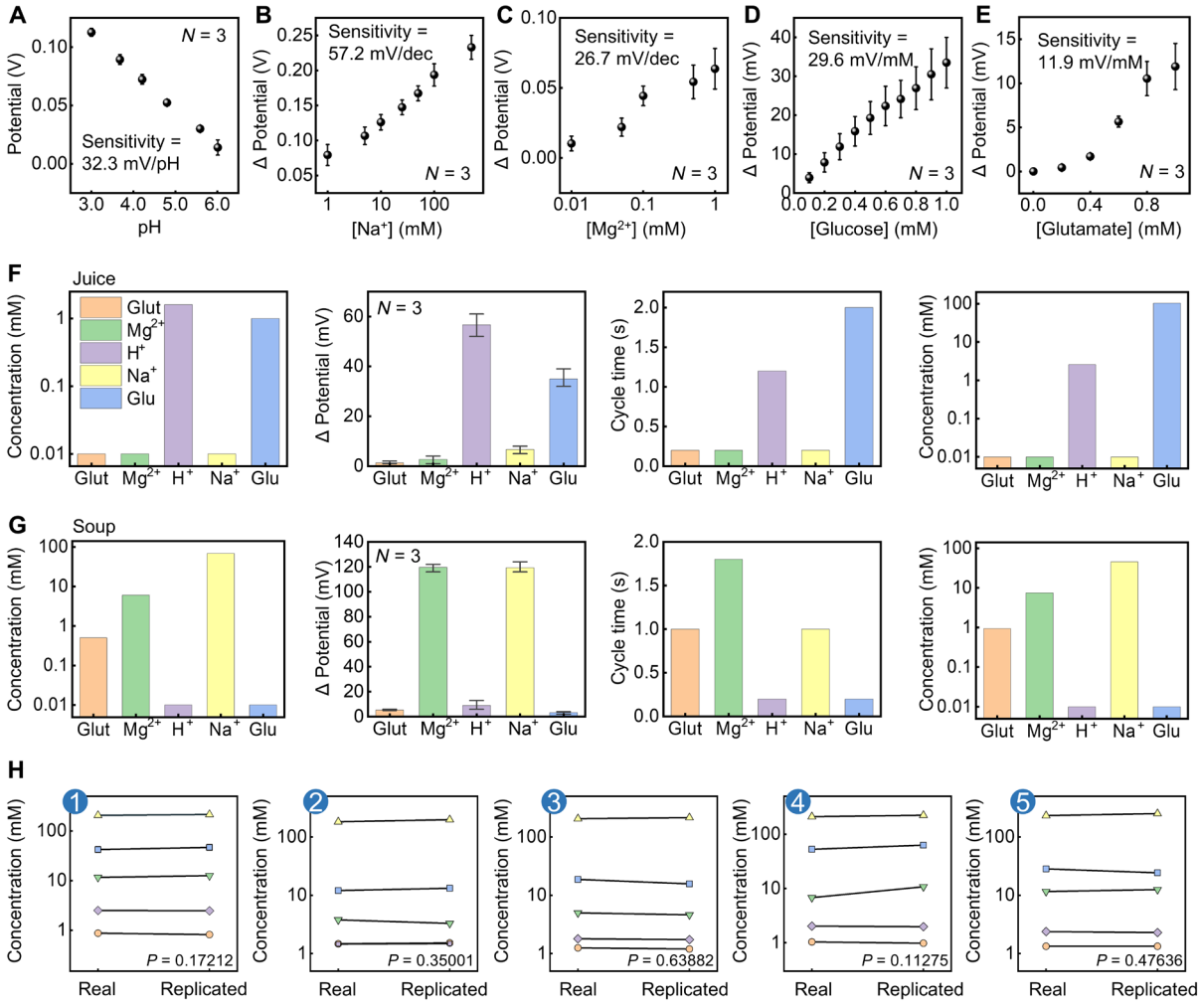

Fig. 4. The electronic tongue for remote acquisition of tastant information. (**A** to **E**) Calibration curves of sensors in the electronic tongue for the five taste-related chemicals. (**F** and **G**) Two illustrative examples ("juice" and "soup") demonstrating the logic flow of the system. The graphs from left to right correspond to the actual concentrations of five taste components in the two liquids, the electrical signals obtained from five sensors, the calculated cycle times (pumping time + interval time) derived from the data for the control of actuators, and the concentrations of the tastants in the replicated solutions measured by electrochemical sensors. For the juice sample, the concentration of glucose in the real solution refers to the value after dilution to match the working range of the sensors. In the third column, a cycle time of less than 1 s indicates that the concentration of the tastant is minimal, meaning the corresponding channel is off. In the fourth column, for the concentration of replicated solutions, a bar below 0.01 mM indicates that the concentration of the corresponding tastant is not measured due to its minimal level in the original solution. (**H**) Comparison of the concentrations of real and replicated solutions across five solution samples with varying combinations of tastants.

(according to Fig. 2, H to L), and the concentrations of the tastants in the replicated solutions measured by electrochemical sensors. Figure S24 presents the raw data of the measurements of the concentrations of five tastants in the replicated solutions, with the calculated concentrations in table S6. The comparison shows consistency with the actual concentrations, thereby verifying the feasibility of this system. It is notable that the time required for the actuation cycle is influenced by the release dynamics of the chemicals from the gel, which depend on both the concentration of the loaded chemicals and their diffusivity. While the sensor measures the chemical concentration in real time, the release speed and diffusion rates of the chemicals from the gel can affect the timing of the actuation process, leading to a potential mismatch between sensor readings and actuation time. Moreover, to illustrate the integration of all system modules, two videos demonstrate the complete process of taste sensing and replication for "chicken" soup and "lemonade," with the device interfacing with a human subject (movie S1). These videos provide a comprehensive view of the functionality of the system in a real-world scenario. It is essential to clarify that for certain foods, the chemicals present in the current system do not encompass the entire spectrum of taste-related compounds. Take chicken soup as an instance: the umami taste relies on a combination of elements, including glutamate, inosinate, guanylate, and a variety of other amino acids (*37*, *38*). While the demonstration here focuses on glutamate, expanding upon this concept by incorporating additional sensors/actuators has the potential to advance the development of more sophisticated virtual taste systems.

A key challenge in taste information capture is fine-tuning the working range of sensors to align with human perception, as most sensors are primarily designed for biosensing applications and have a relatively lower upper detection limit. Therefore, while the sensors

are typically sensitive enough to meet the human perception threshold, a critical issue arises with sensor saturation at high food-relevant concentrations. A specific challenge arises in detecting sweet tastants, since sugar concentrations in sweet foods can reach several hundred millimolar. To deal with this mismatch, a predilution of the target sample by 100 times ensures the alignment for accurate measurement. It is worth noting that if a target sample contains multiple flavors, with one being much more potent than the others, then the dilution process may render the subtler flavors undetectable. To further address this issue, a solution is to implement an algorithm-assisted two-step measurement approach: In the first measurement, the original target sample will be analyzed. An algorithm will serve to identify situations where the concentrations are beyond the detection range. If the concentration of any specific chemical exceeds the detection range, then the system will notify the user on the sensor side that a second measurement should be conducted on that taste chemical, with the sample diluted accordingly. Those sensors that are not saturated will use the results during the first round. This approach will allow for obtaining accurate concentrations of all taste components, ensuring that less intense tastes are not lost despite the need for two measurements. These results further guide the taste reconstruction by multiplying this dilution factor back during actuation to reflect the original concentration. To better illustrate the accuracy and reliability of the e-Taste system, additional experiments involve another five solution samples with varying combinations of tastants (Fig. 4H). Concentration measurements of both real and replicated solutions provide data for quantitative comparison using paired t-tests. The resulting P values indicate no significant differences ($P > 0.05$) between the pairs. Table S7 provides detailed concentration information for each tastant in each test solution, further supporting the quantitative agreement between real and replicated solutions.

Besides this, previous works (*53*) indicate that incorporating a diffusion barrier made of chitosan and polyvinyl chloride (PVC) on the surface of the electrode can prevent sensor saturation and extend the upper limit of detection. As illustrated in fig. S25, after applying the diffusion barrier membrane, the upper limit of detection of the sensor increases from 10 to 21.5 mM. The results demonstrate potential to address the mismatch issue between working range of the sensor and the human perception range. Further improvements may be possible through fine-tuning of the interface structure. It should be noted that the upper limit of glucose detection can depend on multiple factors, such as the design of the electrochemical interfaces and the transducers used. For instance, previous studies have reported upper detection limits of 20 and 100 mM (*54*, *55*). The data on glucose sensing exploration reported in this study aim to provide a potential solution for further improving the performance of the current system through using diffusion barrier materials. Innovations in other sensing methods and the overall multiplexed system include a passive sensing mode based on the two sensing interface designs (enzyme-based and ion-selective membrane based) that eliminates the need of potentiostats for minimizing the power supply. In addition, integrating sensing elements into the multiplexed sensing platform that match tastants within the gustatory interface of this sensor-actuator–coupled HMI system enables real-time operation and interaction with remote environments, which offers a promising solution for individuals to access and experience chemical interactions across space through engagement with digital content.

Human subject tests on single and mixed taste perception

Field testing involves healthy, consenting volunteers instrumented with devices to examine the human perception dimension of the e-Taste system within envisioned application scenarios in the real world. In the first case, assisted by the e-Taste system, it becomes feasible for individuals to share the taste experience of food remotely (Fig. 5A). Figure 5B illustrates an example of transmitting the taste of beverage: When a person immerses the sensor patch in a cup of lemonade near the Golden Gate Bridge (San Francisco, CA, USA), the system uploads the captured concentration data to the IoT platform. The actuator located at the campus of The Ohio State University (Columbus, OH, United States) subsequently downloads the data, guiding to replicate a liquid with the same taste profile. For the remote control and instruction, the entire duration includes the latency (0.3 and 1.4 s for the short- and long-range process, respectively; fig. S26), the sensor response time (~10 s), and an optional signal stabilization time after the response reaches the plateau. Movies S2 and S3 provide additional visual details depicting the process of taste transmission through the ESPNOW communication protocol and IoT platform, respectively.

A human subject test focusing on the sour taste with varying intensity levels serves to demonstrate the accuracy and reliability of this system in taste replication. Arranging the sensors and actuators in different rooms simulates the remote sharing scenario. This test involves three key steps: training subjects to familiarize them with different taste intensities using standard reference solutions, having them taste and rank real (detected by the sensor) and virtual (replicated by the actuator) samples, and analyzing the results to reflect the user perception aspect (Fig. 5C). Figure S27 shows two groups of raw data: one set (left) captured by the pH sensor, and the other (right) used for instructing the actuator. The box plot in Fig. 5D illustrates the original rating data across five sourness intensities, showcasing pairs of real and virtual sourness intensities for comparison. To evaluate the differences between these real and virtual intensities, the study applies a paired sample t test at a 0.05 significance level (degree of freedom = 0). The analysis of virtual versus real taste demonstrates that the differences in very mild (t statistic = −1.8091, $P = 0.1039$), mild (t statistic = 0.0001, $P = 1.0000$), medium (t statistic = 0.8018, $P = 0.4433$), strong (t statistic = 0.4286, $P = 0.6783$), and very strong (t statistic = 0.5571, $P = 0.5911$) intensities show no statistical significance. The result confirms the high accuracy of the system in replicating taste sensations, effectively mimicking the sourness levels encountered in real-world scenarios. Moreover, when comparing across the intensities using one-way analysis of variance (ANOVA), the differences between the five ranks ($F_{9,9} = 44.35$, $P < 0.0001$, $R^2 = 0.82$) show statistical significance. Figure 5E presents a confusion matrix that compares the intensities of real and virtual samples (sample size = 10). This matrix demonstrates an accuracy rate of 70%, indicating that testers can distinguish different sour intensities in the liquids generated by the system. Increasing the training time and providing customized concentration categorization based on individual differences could potentially enhance the accuracy for future applications.

The e-Taste system undergoes further validation test focusing on mixed taste recognition. In the envisioned application scenario, this test assesses the capability of e-Taste to immerse players in the experience of tasting virtual food within a game environment. For example, players might engage in tasks such as manually controlling cooking processes, where stopping a timer accurately allows for

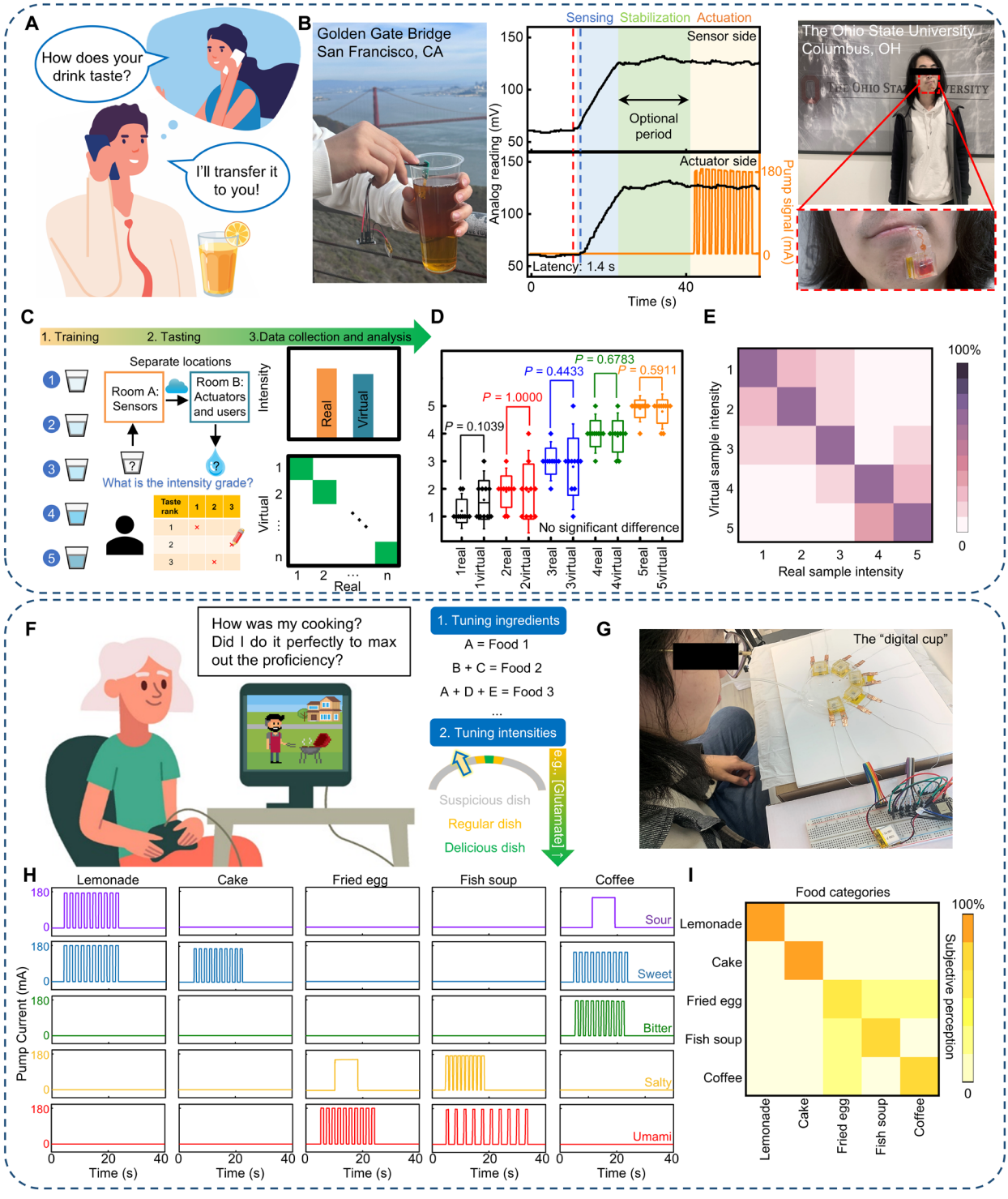

Fig. 5. Field testing results for the assessment of the human perception dimension of e-Taste. (**A**) Schematic illustration showing the function of the e-Taste system in remote taste sharing (images used under license from Adobe Stock). (**B**) Demonstration of using a single-channel device for sharing the taste of beverage over long distances (from California to Ohio in the United States). (**C**) Outline of the procedure for the single taste perception test, including the training, testing, and analysis processes. (**D**) Paired *t* test analysis for statistical validation comparing users' perception to real and virtual samples. The corresponding data are further represented in (**E**) a confusion matrix format. (**F**) Demonstration of using a multichannel system for enhancing taste engagement in immersive gaming. Adjusting the ingredients and associated concentrations can yield various tastes during a cooking game aligned with user's level of cooking proficiency in real time (images used under license from Adobe Stock). (**G**) Photograph of e-Taste in a digital cup design used in the mixed taste recognition test. (**H**) Demonstration of the pump current data used as instruction for simulating five different foods. (**I**) Confusion matrix analyzing the accuracy of the system by comparing the intended food category for the simulation and the user's subjective perception.

reaching the correct cooking stage. Adjusting the concentration and combination of the five tastants can simulate a range of foods with varying levels of cooking (Fig. 5F). During the mixed taste recognition test, subjects interact with a multichannel e-Taste system in a "digital cup" geometry (movie S4). The experiment uses five food options: lemonade, cake, fried egg, fish soup, and coffee. The reference concentrations for the five taste-related chemicals in these foods are from existing literature, as detailed in table S5. Inputting command data for the five tastes based on concentration information and calibration curves of the five actuators guides the generation of the corresponding liquids. After a training session with the reference solutions, subjects taste the liquid generated by the virtual cup and select what food they believe it represents (Fig. 5G). Figure 5H displays the pumping currents used for instructing the actuation process. It is notable that the glutamate concentration used for simulating fish soup (4.93 mM) exceeds the calibration range of the actuation system shown in Fig. 2L (1.362 mM for 1-s interval). To differentiate the taste intensity of umami compared to the solution created using 1-s interval, an extension of the interval time to 2 s enables a further increase in concentration during prolonged interaction. Figure 5I shows a confusion matrix illustrating the recognition outcomes when users taste replicated solutions (sample size: 6, accuracy: 86.7%). The detailed setup for the experiments and the connections of the evaluation board are in figs. S28 and S29, respectively. Together, these examples assess the performance of e-Taste by considering human factors, which further prove its efficacy in bridging the virtual and real environments chemically through digital human-in-the-loop interactions.

DISCUSSION

In summary, this study reports a bio-integrated gustatory interface, e-Taste, for next-generation AR/VR technologies. The coupling between the sensors and actuators through wireless communication modules serves as a unique feature that allows for human chemosensory engagement with the remote world. Systematic studies investigate multiple aspects, including materials selection, integration schemes, design principles, operation logics, implementation framework, and their impacts on the overall performance. While representative, edible chemicals serve to mimic the five basic tastes, this device model can be extended to facilitate the development of more virtual flavor systems by incorporating additional tastants and sensing/actuation modalities encompassing physical cues (e.g., temperature and texture). Tailored designs ensure the safe and reliable operation of the resulting system as a feasible HMI by addressing the need for operation within the oral cavity. Field testing serves to validate the performance of custom designed single- and multichannel devices with a particular emphasis on their accuracy and user perception aspects.

Overall, the findings contribute to establishing design principles for VR/AR systems incorporating chemical signals/components, a relatively unexplored research field. The gustatory interface will pave the way for a new era of AR/VR systems with chemical components by allowing users not only to visualize and hear virtual environments but also to taste them. This will elevate immersion levels and lay the groundwork for the "Metaverse." Potential applications include immersive gaming, online shopping, remote education, weight management, sensory testing, physical rehabilitation, and others. For example, sensory loss, particularly gustatory and olfactory impairments, represents a challenge for individuals with traumatic brain injuries (TBIs) (*56*, *57*) and patients with long-haul COVID (*58*). Accordingly, addressing this issue within the patient population using e-Taste can notably improve the nutritional intake, overall recovery, and the quality of life.

When coupled with its sensing capabilities, e-Taste can further facilitate interaction with distant realms. For example, it can promote accessibility and inclusivity by enabling individuals with disability for social activity engagement through virtual participation. In food industry, e-Taste can enable cost-effective tasting remotely for refining food and beverage formulations. The virtual communication capability will promote global collaborations and feedback. On the basis of the preliminary prototype reported here, immediate opportunities lie in deploying fully bio-integrated gustatory displays, conducting user studies to assess the individual experience and social acceptance, as well as incorporating additional operation modalities to complete the flavor gestalts. Beyond focusing on chemical signals in food, the digital coupling between sensors and actuators for signal encoding, storage, transmission, and decoding extends to alternative scenarios such as chemical message delivery in defense and drug administration in the medical field. Together, these fundamental research outcomes provide fertile ground for the development of new products that enable people and other living systems to interact with the world through chemical signals in the digital era.

Moreover, because of its spatial targeting capability, the system can potentially enable the investigation of how different areas of the tongue respond to the same solution as well as how variations in solution intensity and composition influence human perception. These findings will provide a deeper understanding of how the brain processes sensory signals from the oral cavity. Figure S30 illustrates the device applied to different regions of the tongue, demonstrating the capability to investigate how various locations respond to identical taste solutions. The accompanying square wave plots demonstrate precise control over taste intensity with a temporal resolution, highlighting its potential for detailed studies of gustatory pathways and human taste perception. The system allows for a range of chemosensory tests, including (i) threshold test, where the concentration of a tastant is gradually increased until it becomes perceptible, achieved by tuning the duty cycle of the actuation square waves; (ii) adaptation test, where a solution is delivered continuously to a specific area of the tongue to allow subjects to report perceived intensity changes over time, providing insights into sensory adaptation; and (iii) binary mixture suppression test, where one tastant is delivered followed by another to assess whether the intensity of the first taste diminishes, revealing potential interactions between different tastants. It should be noted that while our current platform provides a gustatory interface enabling liquid delivery to the oral cavity in a quantitatively controllable manner, the demonstration here aims to suggest a future direction that is not yet ready for biomedical research in chemosensory testing. It is necessary to further consider factors such as different taste sensations beyond this study (e.g., fat, astringency, spiciness, and complex tastes), the variation among individuals, and the involvement of neural activities. Future directions should include: (i) validation across a statistically meaningful population with diverse taste profiles, including those with ageusia, to understand the distribution of perception; (ii) the application of reinforcement learning to personalize and optimize actuation patterns for maximizing recognition rates and minimizing response times; and (iii) the exploration of associations between taste perception,

other sensations, and cognitive activities to gain insights into gustatory pathways.

Moving forward, several enhancements and strategic developments can address the existing limitations and expand the capabilities of the system. (i) While the sensing interfaces demonstrate selectivity, tastants can still interfere with each other in complex environments containing multiple chemicals. A potential solution is to apply a cross-sensitivity model, as reported in previous studies, to further address this issue caused by nonspecific interactions. This model assumes that the response of a sensor in a complex environment is the sum of responses to specific and nonspecific interactions, and calibration using the sensitivity matrix can separate the two types of signals (*59*, *60*). (ii) Moreover, the current system has a limitation regarding residue left in the channel after each pump cycle. To address this, this work reports a refillable structure to refresh the channel after every use. In addition, calculating residue to adjust concentrations for subsequent actuation cycles is also a feasible method. Besides that, another potential solution using this actuator model is to eliminate design with hydrogels and preload a concentrated liquid and water into separate channels. By individually controlling the two channels, the concentration can be precisely adjusted, and the water channel can flush the mixing zone after each use, ensuring that the system remains clean and ready for subsequent actuation cycles. (iii) On the other hand, note that human sensation of taste intensity is theoretically continuous and does not follow a linear relationship with tastant concentration. Previous studies suggest that human perception can be approximated by the Stevens' power law (*61*), which describes an exponential relationship between tastant concentration and perception, expressed as $\psi(I) = kI^a$ [where I is the stimulus intensity, $\psi(I)$ is the sensation magnitude, a is an exponent based on the sensory modality, and k is a proportionality constant based on the units used]. Note that for the perception of acidity levels, the values of k and a are still under exploration. Therefore, future research requires further efforts in establishing taste perception models through rigorous field testing with large populations by referring to the Steven's power law and fine-tuning the working range of actuators to provide a continuous concentration range that aligns with human perception.

MATERIALS AND METHODS

Fabrication and characterization of tastant-loaded hydrogels

The mixture of the monomer (hydroxyethyl)methacrylate (1.45 ml), ethylene glycol dimethacrylate (5 μl) as a crosslinker, photo-initiator 2-hydroxy-2-methylpropiophenone (Darocur) (9 mg), deionized (DI) water (0.5 ml), and taste chemicals, underwent a 20-min polymerization process upon irradiation under UV light at 365 nm, resulting in the formation of the hydrogel loaded with taste chemicals. Establishing an overnight period at room temperature for the resultant crosslinked system facilitated water evaporation. Subjecting the crosslinked gels, loaded with concentrated taste chemicals, to solutions for a specific duration and quantifying the amount of taste chemicals that have diffused into the solution offered a quantitative assessment of the performance of the release media (fig. S31).

Fabrication of the EM actuation system

Figure S3 illustrates the fabrication process of the EM actuation system, including three key functional parts in total: (i) Microfluidic channel, the fabrication of the microfluidic channel began with creating a silicon mold using photolithography followed by deep reactive ion etching (Plasma Therm SLR770) down for 200 μm. Spin casting a layer of polymethylmethacrylate (PMMA A5, KemLab; at 3000 rpm for 30 s, followed by curing at 180°C for 10 min) onto the mold aided in the easy release of PDMS post-casting and curing. Mixing and pouring the base and curing agent (ratio: 10:1) of PDMS (Sylgard 184, Dow Corning) onto the silicon mold, then spin coating at 350 rpm for 1 min and curing at 100°C formed the top layer of the soft microfluidic channel with a thickness of 250 μm; then spin coating PDMS onto a plain silicon mold at 800 rpm for 1 min and curing at 100°C created the capping layer with a thickness of 75 μm; and placing tastant-infused gel onto the reservoir, punching holes in these layers with circular punchers for inlets and outlets, together with joining the patterned top layer to the capping layer after ozone plasma treatment, completed the fabrication of the microfluidics. (ii) Minipump, the fabrication of the minipump began with a cut-and-paste method, cutting polyimide (PI) tape (thickness: 0.12 mm, Edge Scientific) into 1 cm by 1 cm and stacking them onto the surface of a Petri dish created an easy-released mold (height: 2.5 mm in total), pouring PDMS onto the mold and curing at 80°C overnight constructed the bottom base of the minipump, spin coating PDMS onto a plain silicon mold at 800 rpm for 1 min and curing at 100°C created the deformable membrane (thickness: 75 μm), and clamping NdFeB permanent magnets (3 mm by 3 mm, thickness: 0.5 mm; Supermagnetman, M0350) onto both sides of the membrane, punching holes on the surface of minipump with circular punchers for the outlet (diameter: 1.0 mm) and inlet (diameter: 0.4 mm), together with joining the deformational membrane to the bottom base after ozone plasma treatment, completed the fabrication of the minipump. (iii) Coil chamber, the same cut-and-paste method, followed by pouring and curing of PDMS served to make the coil chamber, winding magnetic wire (diameter: 0.05 mm, Elektrisola, P155) around a coil former (DigiKey, diameter: 4 mm) yielded the EM coil, and last, fixing the coil (diameter: 4 mm, 250 turns) onto the assembling cap with PDMS followed by extending the two ends of the wire into the actuating circuit (note S2) completed fabrication of the coil chamber part. (iv) Assembling the three parts together following another ozone plasma treatment concluded the preparation of the EM actuation system. The fabrication of the microfluidics for liquid routing, mixing, and delivery followed the same procedures. Figure S2 provides comprehensive dimensions for all elements of the microfluidic system, in which the channel height of microfluidic channel is 200 μm.

The results depicted in Figs. 1 to 3 used analytical-grade silicone and taste chemicals sourced from Sigma-Aldrich to accurately assess the performance of the sensing and actuation devices. To ensure food safety, in human subject tests, SORTA-Clear 37 (Smooth-On), a food-grade silicone, replaced PDMS to mold all the components. Because SORTA-Clear 37 has a higher viscosity, the spin-coating speeds for the channel layer and capping layer increased to 800 and 1200 rpm, respectively. In addition, the taste chemicals used were switched to food-grade alternatives. Table S8 includes all the food-grade materials used in the human subject tests. All the other steps remained the same.

Refilling of the tastant-infused gels

Replenishing the tastant-infused gels enhanced the reusability of the microfluidic channel. This process began with creating a half-circle opening at the reservoir using circular punchers to establish a refilling

port. Subsequently, removing the used gel and inserting a new one refreshed the system after each pumping process. Sealing the opening with a scotch tape completed the refilling process.

Characterization of the EM actuation system

To characterize the microfluidic system for liquid delivery, a DC power supply generated a voltage ranging from 0 to 5 V. The corresponding current passing through the coil ranged from 0 to 260 mA. A camera captured the deformation of the thin-film deformational membrane under varying currents. Concurrently, a thermometer (Fluke) recorded temperature variations over time at different current levels, as shown in Fig. 2G. A pipette with a range of 10 to 100 μl served for volume measurements in Fig. 2F. Setting the current at 180 mA ($V = 3.3$ V) and integrating it with an "on/off" switch circuit facilitated the collection of data regarding five taste chemicals at varied interval times. The concentrations of these chemicals were determined using a pH meter and specific assay kits for Mg^{2+}, Na^{+}, glucose, and glutamate (Elabscience). Standard curves for the four kinds of assay kits are in fig. S32.

To evaluate the electrical, thermal, and mechanical stability of the system, a DC power supply provided a consistent 3.7 V source, with an Arduino connected to a computer controlling the pulse width and duty cycle of the base current for the BJT as the on/off switch. This setup directed an actuating PWM (pulse width: 1 s, 50% duty cycle) across the EM coil. An electrochemical workstation (PalmSens4, CA, USA) captured the voltage signals, while a Power Profile Kit (Nordic Semiconductor) captured the current signals, as shown in Figs. 2 (D and E) and 3 (C and D). For the thermal stability tests outlined in fig. S11A, the system underwent placement on a hot plate with varied temperature settings (25°C, 37°C). The Arduino software managed the PWM parameters (pulse width: 1 s; duty cycles: 50, 55.56, 62.5, 71.43, 83.33, and 100%), while a pH meter measured the H^{+} concentration in produced solutions. A thermometer gathered the temperature data in fig. S11B at 50% duty cycle PWM, while a Thermal Imaging Camera (Flir One) captured the data presented in Fig. 3G.

EM simulation

The coil generates EM field encompassing the surrounding environments. To evaluate the EM safety of the system, the simulations were performed using the commercial software Ansys Maxwell to determine the magnetic flux density distributions around the coil and the Lorentz force F_{mag} acting on the magnet based on the dimensions depicted in fig. S2, where a current of 180 mA was applied to the coil. An adaptive mesh (maximum element size of 0.5 mm) was adopted to ensure computational accuracy. The electromagnetic parameters of PDMS and coil (250 turns) in the material library of Ansys Maxwell were used in the simulation.

Mechanical simulation

To evaluate the mechanical properties of the system, The FEA commercial software ABAQUS was used to study the deformation and corresponding strain distributions of the channel with typical bending and twisting and the force F_{film} acting on the magnet from the PDMS film. Definition of the PDMS microfluidic channel was based on the dimension depicted in fig. S2. The hexahedral elements (C3D8R) with minimum mesh size 0.05 mm were adopted, and the convergence of finite element analysis was tested. The elastic modulus and Poisson's ratio used in the analysis were 2.85 MPa and 0.49 for PDMS, respectively. F_{mag} (see the method in the "EM simulation" section) and F_{film} were used to determine the balance position of the magnet for the pump with current ON (Fig. 3E).

Fabrication, characterization, and calibration of sensors for detection of five taste chemicals

JLCPCB produced the PI-based gold thin-film patches, designed with PI passivation on top, leaving eight electrode areas (2 mm in diameter) exposed for functionalization.

Fabrication of the PANI working electrodes (WEs) for pH sensing started by performing cyclic voltammetry in 0.25 M aniline solution (in 0.5 M H_2SO_4, Sigma-Aldrich), ranging from 0.2 to 1 V for 10 cycles. The reference electrode (RE) used was Ag/AgCl. A platinum (Pt) wire served as the counter electrode.

Preparation of polymeric ISMs used the following recipes: (i) Na^{+}-ISM: sodium ionophore X [1 weight % (wt %)], sodium tetrakis[3,5-bis(trifluoromethyl)-phenyl] borate (0.55 wt %), PVC (33 wt %), and bis(2-ethylhexyl) sebacate (65.45 wt %) (Sigma-Aldrich). Dissolving 100 mg of the mixture in 660 μl of tetrahydrofuran formed the Na^{+} ISM cocktail. (ii) Mg^{2+}-ISM: magnesium ionophore I (1.4 wt %), potassium tetrakis(4-chlorophenyl) borate (1 wt %), PVC (33 wt %), and 2-nitrophenyloctylether (64.5 wt %) (Sigma-Aldrich). Dissolving 100 mg of the mixture in 660 μl of tetrahydrofuran formed the Mg^{2+} ISM cocktail. Casting these mixtures on the gold thin film electrodes and drying the system overnight completed the preparation of ISM-functionalized sensing interfaces.

Fabrication of the thin-film Ag/AgCl RE started with coating the gold thin-film electrode with silver epoxy (Chemtronics CW2400) and curing it at room temperature overnight. Soaking the electrode in sodium hypochlorite solution (5 wt %) for 1 hour converted the surface to AgCl. Homogenizing 438 mg of polyvinyl butyral (10 wt %) and 250 mg of KCl powder in 5 ml of anhydrous ethanol through ultrasonication formed the solid electrolyte coating solution. Drop casting the solid electrolyte coating solution onto the Ag/AgCl and drying overnight concluded the process.

The glucose and glutamate sensors underwent fabrication following a similar process, differing only in the enzyme type and concentration. For the anode, the fabrication began with electrodeposition of platinum black onto the gold electrode through cyclic voltammetry using an Ag/AgCl RE and a Pt wire as the counter electrode. The procedure involved placing a mixture of 3 wt % chloroplatinic acid ($PtCl_6H_2$; Sigma-Aldrich, MO, USA) and 0.1 wt % lead acetate [$Pb(C_2H_3O_2)]_2$; Sigma-Aldrich, MO, USA] on the gold electrode before voltammetry, which ran from −0.4 to 0.1 V at a scan rate of 0.1 V/s over five scans. Subsequent to this, the process involved suspending tetrathiafulvalene (183180, Sigma-Aldrich) in a 1:9 volume-to-volume mixture of acetone and ethanol and then applying 5 μl of this suspension onto the Pt black surface, allowing it to dry for an hour. Mixing 875 μl of DI water, 125 μl of a 0.5 wt % glutaraldehyde solution in DI water, and 20 mg of BSA (BP9700100, Thermo Fisher Scientific) yielded the BSA solution, which rested for 30 min. Dissolving freeze-dried enzymes in a 1× PBS formed solutions of GlutOx (31.25 U/ml; YMS-80049, CosmoBio, USA) and GOx (40 mg/ml; Sigma-Aldrich, MO, USA). Adding 5 μl of a 1:1:2 volume-to-volume mixture of the enzyme solution, BSA solution, and 1× PBS with Nafion 117 (1 wt %) (292567, Sigma-Aldrich) to the Pt black surface and drying at 4°C for a day completed the anode preparation.

For the cathode, the fabrication began with the same step of electrodeposition of platinum black onto the gold electrode through cyclic

voltammetry, followed by dropping 5 μl of 10% platinized carbon suspended in a 2% ethanolic suspension of Nafion 117 (PTC, 205958, Sigma-Aldrich) solution onto the electrode and drying for 30 min.

Sensor calibration involved measuring the open circuit potential (OCP) between the two electrodes (i.e., WE and RE of the ion sensors, cathode, and anode of the glucose/glutamate sensors) using an electrochemical workstation (PalmSens4, CA, USA). The load resistance for the glucose and glutamate sensors was 4.2 megohm. This measurement took place after incubating the electrodes in varied concentrations of five taste chemicals (H^+: pH 3.0 to 6.0; Na^+: 1 mM to 1 M; Mg^{2+}: 0.01 to 1 mM; glucose: 0.1 to 1.0 mM; glutamate: 0 to 1.0 mM). Plotting the OCP values against these concentrations formed the calibration curves.

Preparation of the diffusion barrier

Drop-casting and drying 2 μl of 1 wt % chitosan suspension prepared in 0.1 M acetic acid onto the anode electrode of glucose sensor formed a polymeric membrane first. Dipping the electrode into the chitosan solution for 5 s and allowing them to dry then created an additional encapsulation. Dipping the pads for 5 s in a 3 wt % PVC suspension in tetrahydrofuran and thoroughly air-drying them lastly formed the outer PVC membrane layer, completing the fabrication of the diffusion barrier (*53*).

Operation of the integrated e-Taste system incorporating sensors and actuators

The voltage outputs from five taste chemical sensors, one RE, and two cathodes on the biosensing patch were initially captured by both the built in ADC on ESP32-C3 and a separate ADC board (ADS1115) and converted into numerical values. These data were relayed to the ESP32-C3 MCU via five input/output (IO) ports and the I2C bus linked to ADC. Following this conversion, the ESP32-C3 MCU processed the data by computing a rolling average, taking each set of 100 consecutive data points in an overlapping manner (for instance, averages of points 1 to 100, 2 to 101, 3 to 102, and so forth, with each data point representing 10 ms), and then wirelessly transmitted the data. For short-range communication, the system used ESPNOW, a basic wireless communication protocol embedded in the ESP32 board to establish direct connections through the unique MAC address for each device. The long-range transmission mode used an IoT platform (Blynk). Leveraging its cloud connectivity enabled data exchange over wider distances through MAC addresses. In this setup, the ESP32-C3 sender unit on the sensor side interfaced with the Internet through Wi-Fi using a specific username and password and sent data to the Blynk website. Similarly, connecting the ESP32-C3 receiver on the actuator side to Wi-Fi enabled it to access the Blynk website to retrieve the transmitted data.

Upon receiving the data, the paired ESP32-C3 receiver unit interpreted these signals, converting them into PWM signals (note S4). These were then dispatched through five analog pins (A0, A1, A2, A4, and A5) to the bases of five BJTs in the circuit of the minipump. The minipumps, powered by LiPo batteries (3.7 V, 100 mAh; 402020, Amazon), facilitated precise fluid control as per the received instructions. The control board registered a longer interval time between PWM output to the corresponding actuators when exposed to higher concentrations. This led to an extended interaction time with the gels, contributing to enhanced chemical release. Note S2 further detailed operational specifics of the EM minipump and its integration within the system.

Human subject test

Human subject studies followed a protocol approved by the Institutional Review Board at The Ohio State University (study number: 2023H0272), with informed written consents obtained before the field testing. The studies on single taste perception and mixed taste recognition involved 10 volunteers (3 female and 7 male) and 6 volunteers (2 female and 4 male) separately, aged between 20 and 45 years old, to verify the feasibility of this system.

Single taste perception test

A 50-min preliminary training (10 min for each intensity) involved each participant sampling five cups of citric acid with varying acid intensities, labeled as very mild, mild, medium, strong, and very strong (corresponding ranking score: 1, 2, 3, 4, and 5). The actual concentrations achieved by the actuators (by varying the interval time from 0.2 to 1.0 s) served as the five discrete acidity levels used in this work. Accordingly, the system algorithm correlated these five discrete levels with the corresponding signals captured by the pH sensors. As an initial step toward future research, this categorization facilitated a qualitative assessment of the functionality and efficacy of e-Taste in taste replication and simulation through field testing, where participants were aware that there were five distinct categories before the test.

During the experiment, participants encountered five pairs of citric acid solutions. Each pair consisted of a sample with a predetermined acid concentration and a corresponding sample generated by the minipump, replicating the concentration data transmitted from the biosensor patch. Participants tasted all the samples in a random sequence, with a minimum 5-min interval for mouth cleansing with DI water between each. They then assessed and ranked the sourness intensity of each sample, referencing the five levels experienced during the training. The data were analyzed in Origin software with paired-sample *t* tests to assess whether there was a significant difference in perceived intensity between the real and replicated (e.g., virtual) samples. A confusion matrix (real versus virtual) evaluated the accuracy of replication.

Mixed taste recognition

This test involved preparing solutions with distinct tastes by varying combinations of the five food-grade taste chemicals to represent various food profiles, including lemonade, cake, fried egg, coffee, and fish soup. Participants underwent a 1-hour training session (10 min for usage instruction, 10 min for each food) to acquaint themselves with these specific tastes. In the remote tasting trials, they engaged with the multichannel actuation device, the "digital cup," placing the mouthpiece on their tongues to simulate the tastes determined from authoritative literatures. Following each tasting experience, participants cleansed their mouth with DI water and then identified the food taste they perceived. A confusion matrix evaluated the accuracy of recognition by correlating the taste categories and subjective perceptions.

Supplementary Materials

The PDF file includes:

Supplementary Notes S1 to S4
Figs. S1 to S32
Tables S1 to S8
Legends for movies S1 to S4
Legend for data S1
References

Other Supplementary Material for this manuscript includes the following:

Movies S1 to S4
Data S1

REFERENCES AND NOTES

1. Y. Liu, C. Yiu, Z. Song, Y. Huang, K. Yao, T. Wong, J. Zhou, L. Zhao, X. Huang, S.K. Nejad, M. Wu, D. Li, J. He, X. Guo, J. Yu, X. Feng, Z. Xie, X. Yu, Electronic skin as wireless human-machine interfaces for robotic VR. *Sci. Adv.* **8**, eabl6700 (2022).
2. X. Yu, Z. Xie, Y. Yu, J. Lee, A. Vazquez-Guardado, H. Luan, J. Ruban, X. Ning, A. Akhtar, D. Li, B. Ji, Y. Liu, R. Sun, J. Cao, Q. Huo, Y. Zhong, C. Lee, S. Kim, P. Gutruf, C. Zhang, Y. Xue, Q. Guo, A. Chempakasseril, P. Tian, W. Lu, J. Jeong, Y. Yu, J. Cornman, C. Tan, B. Kim, K. Lee, X. Feng, Y. Huang, J. A. Rogers, Skin-integrated wireless haptic interfaces for virtual and augmented reality. *Nature* **575**, 473–479 (2019).
3. M. Zhu, Z. Sun, Z. Zhang, Q. Shi, T. He, H. Liu, T. Chen, C. Lee, Haptic-feedback smart glove as a creative human-machine interface (HMI) for virtual/augmented reality applications. *Sci. Adv.* **6**, eaaz8693 (2020).
4. S. Liu, K. Ma, B. Yang, H. Li, X. Tao, Textile electronics for VR/AR applications. *Adv. Funct. Mater.* **31**, 2007254 (2021).
5. T. Jin, Z. Sun, L. Li, Q. Zhang, M. Zhu, Z. Zhang, G. Yuan, T. Chen, Y. Tian, X. Hou, C. Lee, Triboelectric nanogenerator sensors for soft robotics aiming at digital twin applications. *Nat. Commun.* **11**, 5381 (2020).
6. F. Wen, Z. Sun, T. He, Q. Shi, M. Zhu, Z. Zhang, L. Li, T. Zhang, C. Lee, Machine learning glove using self-powered conductive superhydrophobic triboelectric textile for gesture recognition in VR/AR applications. *Adv. Sci.* **7**, 2000261 (2020).
7. A. Sarasola-Sanz, N. Irastorza-Landa, E. López-Larraz, C. Bibián, F. Helmhold, D. Broetz, N. Birbaumer, A. Ramos-Murguialday, A hybrid brain-machine interface based on EEG and EMG activity for the motor rehabilitation of stroke patients,in *Proceedings of the 2017 International Conference on Rehabilitation Robotics* (ICORR) (IEEE, 2017), pp. 895–900.
8. Y. Yu, J. Nassar, C. Xu, J. Min, Y. Yang, A. Dai, R. Doshi, A. Huang, Y. Song, R. Gehlhar, A. D. Ames, W. Gao, Biofuel-powered soft electronic skin with multiplexed and wireless sensing for human-machine interfaces. *Sci. Robot.* **5**, eaaz7946 (2020).
9. K. He, Y. Liu, M. Wang, G. Chen, Y. Jiang, J. Yu, C. Wan, D. Qi, M. Xiao, W. R. Leow, H. Yang, M. Antonietti, X. Chen, An artificial somatic reflex arc. *Adv. Mater.* **32**, e1905399 (2020).
10. W. Ding, A. C. Wang, C. Wu, H. Guo, Z. L. Wang, Human–machine interfacing enabled by triboelectric nanogenerators and tribotronics. *Adv. Mater. Technol.* **4**, 1800487 (2019).
11. R. Cao, X. Pu, X. Du, W. Yang, J. Wang, H. Guo, S. Zhao, Z. Yuan, C. Zhang, C. Li, Z. L. Wang, Screen-printed washable electronic textiles as self-powered touch/gesture tribo-sensors for intelligent human–machine interaction. *ACS Nano* **12**, 5190–5196 (2018).
12. Y. Yu, J. Li, S. A. Solomon, J. Min, J. Tu, W. Guo, C. Xu, Y. Song, W. Gao, All-printed soft human-machine interface for robotic physicochemical sensing. *Sci. Robot.* **7**, eabn0495 (2022).
13. J. Yin, R. Hinchet, H. Shea, C. Majidi, Wearable soft technologies for haptic sensing and feedback. *Adv. Funct. Mater.* **31**, 2007428 (2021).
14. Y. Huang, J. Zhou, P. Ke, X. Guo, C. K. Yiu, K. Yao, S. Cai, D. Li, Y. Zhou, J. Li, T. H. Wong, Y. Liu, L. Li, Y. Gao, X. Huang, H. Li, J. Li, B. Zhang, Z. Chen, H. Zheng, X. Yang, H. Gao, Z. Zhao, X. Guo, E. Song, H. Wu, Z. Wang, Z. Xie, K. Zhu, X. Yu, A skin-integrated multimodal haptic interface for immersive tactile feedback. *Nat. Electron.* **6**, 1020–1031 (2023).
15. J. Park, D. H. Kang, H. Chae, S. K. Ghosh, C. Jeong, Y. Park, S. Cho, Y. Lee, J. Kim, Y. Ko, J. J. Kim, H. Ko, Frequency-selective acoustic and haptic smart skin for dual-mode dynamic/static human-machine interface. *Sci. Adv.* **8**, eabj9220 (2022).
16. H. Oh, G. C. Yi, M. Yip, S. A. Dayeh, Scalable tactile sensor arrays on flexible substrates with high spatiotemporal resolution enabling slip and grip for closed-loop robotics. *Sci. Adv.* **6**, eabd7795 (2020).
17. M. Wang, Z. Yan, T. Wang, P. Cai, S. Gao, Y. Zeng, C. Wan, H. Wang, L. Pan, J. Yu, S. Pan, K. He, J. Lu, X. Chen, Gesture recognition using a bioinspired learning architecture that integrates visual data with somatosensory data from stretchable sensors. *Nat. Electron.* **3**, 563–570 (2020).
18. H. Luo, J. Du, P. Yang, Y. Shi, Z. Liu, D. Yang, L. Zheng, X. Chen, Z. L. Wang, Human–machine interaction via dual modes of voice and gesture enabled by triboelectric nanogenerator and machine learning. *ACS Appl. Mater. Inter.* **15**, 17009–17018 (2023).
19. Z. Sun, Z. Zhang, C. Lee, A skin-like multimodal haptic interface. *Nat. Electron.* **6**, 941–942 (2023).
20. M. Zhu, Z. Sun, C. Lee, Soft modular glove with multimodal sensing and augmented haptic feedback enabled by materials' multifunctionalities. *ACS Nano* **16**, 14097–14110 (2022).
21. Z. Sun, M. Zhu, X. Shan, C. Lee, Augmented tactile-perception and haptic-feedback rings as human-machine interfaces aiming for immersive interactions. *Nat. Commun.* **13**, 5224 (2022).
22. A. Chalmers, D. Zholzhanova, T. Arun, A. Asadipour, Virtual flavor: High-fidelity simulation of real flavor experiences. *IEEE Comput. Graph. Appl.* **43**, 23–31 (2023).
23. S. Hariri, N. A. Mustafa, K. Karunanayaka, A. D. Cheok, Electrical stimulation of olfactory receptors for digitizing smell, in *Proceedings of the 2016 Workshop on Multimodal Virtual and Augmented Reality* (Association for Computing Machinery, 2016), pp. 1–4.
24. H. Miyashita, Norimaki synthesizer: Taste display using ion electrophoresis in five gels, in *Extended Abstracts of the 2020 CHI Conference on Human Factors in Computing Systems* (Association for Computing Machinery, 2020), pp. 1–6.
25. Y. H. Jung, B. Park, J. U. Kim, T. I. Kim, Bioinspired electronics for artificial sensory systems. *Adv. Mater.* **31**, e1803637 (2019).
26. M. Cuartero, A. Carretero, M. S. García, J. A. Ortuño, New potentiometric electronic tongue for analyzing teas and infusions. *Electroanalysis* **27**, 782–788 (2015).
27. M. Del Valle, Materials for electronic tongues: Smart sensor combining different materials and chemometric tools, in *Materials for Chemical Sensing* (Springer International Publishing AG, 2017), pp. 227–265.
28. R. B. Domínguez, L. Moreno-Barón, R. Muñoz, J. M. Gutiérrez, Voltammetric electronic tongue and support vector machines for identification of selected features in Mexican coffee. *Sensors* **14**, 17770–17785 (2014).
29. N. Ranasinghe, Virtual taste: Digital simulation of taste sensations via electric, thermal, and hybrid stimulations. *Multimed. Tools Appl.* **83**, 56517–56548 (2023).
30. T. Delompré, E. Guichard, L. Briand, C. Salles, Taste perception of nutrients found in nutritional supplements: A review. *Nutrients* **11**, 2050 (2019).
31. B. Piqueras-Fiszman, C. Spence, *Multisensory flavor perception: From fundamental neuroscience through to the marketplace* (Woodhead Publishing, 2016), 376 pp.
32. J. Yunas, M. M. Said, R. E. Pawinanto, B. Bais, B. Mulyanti, I. Hamidah, A. B. D. Nandiyanto, B. Y. Majlis, Magnetic polymer-based micropumps for microfluidic sample delivery system. *J. Adv. Res. Fluid Mech. Therm. Sci.* **85**, 12–21 (2021).
33. G. M. Brosvic, W. W. McLaughlin, Quality specific differences in human taste detection thresholds as a function of stimulus volume. *Physiol. Behav.* **45**, 15–20 (1989).
34. Wikipedia contributors. "Drop (unit)." Wikipedia, The Free Encyclopedia, December 12, 2023. https://en.wikipedia.org/wiki/Drop_(unit).
35. Wikipedia contributors. "Taste detection threshold." Wikipedia, The Free Encyclopedia, November 27, 2023. https://en.wikipedia.org/wiki/Taste_detection_threshold.
36. M. C. Cornelis, A. El-Sohemy, Coffee, caffeine, and coronary heart disease. *Curr. Opin. Lipidol.* **18**, 13–19 (2007).
37. T. Nishimura, S. Goto, K. Miura, Y. Takakura, A. S. Egusa, H. Wakabayashi, Umami compounds enhance the intensity of retronasal sensation of aromas from model chicken soups. *Food Chem.* **196**, 577–583 (2016).
38. Umami Information Center. Umami. https://zh-cn.umamiinfo.com/richfood/foodstuff/seafood.
39. National Institutes of Health (NIH). Magnesium. https://ods.od.nih.gov/factsheets/Magnesium-HealthProfessional.
40. MyFoodData. Glucose. www.myfooddata.com/articles/high-sugar-foods.
41. S. R. Calliope, N. C. Samman, Sodium content in commonly consumed foods and its contribution to the daily intake. *Nutrients* **12**, 34 (2019).
42. W. Jeon, C. B. Shin, Design and simulation of passive mixing in microfluidic systems with geometric variations. *Chem. Eng. J.* **152**, 575–582 (2009).
43. J. T. Reeder, J. Choi, Y. Xue, P. Gutruf, J. Hanson, M. Liu, T. Ray, A. J. Bandodkar, R. Avila, W. Xia, S. Krishnan, S. Xu, K. Barnes, M. Pahnke, R. Ghaffari, Y. Huang, J. A. Rogers, Waterproof, electronics-enabled, epidermal microfluidic devices for sweat collection, biomarker analysis, and thermography in aquatic settings. *Sci. Adv.* **5**, eaau6356 (2019).
44. A. Koh, D. Kang, Y. Xue, S. Lee, R. M. Pielak, J. Kim, T. Hwang, S. Min, A. Banks, P. Bastien, M. C. Manco, L. Wang, K. R. Ammann, K. I. Jang, P. Won, S. Han, R. Ghaffari, U. Paik, M. J. Slepian, G. Balooch, Y. Huang, J. A. Rogers, A soft, wearable microfluidic device for the capture, storage, and colorimetric sensing of sweat. *Sci. Transl. Med.* **8**, 366ra165 (2016).
45. Magnets safety (Stanford Magnets, 2024); www.stanfordmagnets.com/are-magnets-dangerous.html.
46. B. Ciui, A. Martin, R. K. Mishra, T. Nakagawa, T. J. Dawkins, M. Lyu, C. Cristea, R. Sandulescu, J. Wang, Chemical sensing at the robot fingertips: Toward automated taste discrimination in food samples. *ACS Sens.* **3**, 2375–2384 (2018).
47. Blynk. (© 2025 Blynk Technologies Inc). https://blynk.io/.
48. L. Yin, J. M. Moon, J. R. Sempionatto, M. Lin, M. Cao, A. Trifonov, F. Zhang, Z. Lou, J. M. Jeong, S. J. Lee, S. Xu, J. Wang, A passive perspiration biofuel cell: High energy return on investment. *Joule* **5**, 1888–1904 (2021).
49. J. Lv, L. Yin, X. Chen, I. Jeerapan, C. A. Silva, Y. Li, M. Le, Z. Lin, L. Wang, A. Trifonov, S. Xu, S. Cosnier, J. Wang, Wearable biosupercapacitor: Harvesting and storing energy from sweat. *Adv. Funct. Mater.* **31**, 2102915 (2021).
50. Y. Luo, M. R. Abidian, J. H. Ahn, D. Akinwande, A. M. Andrews, M. Antonietti, Z. Bao, M. Berggren, C. A. Berkey, C. J. Bettinger, J. Chen, P. Chen, W. Cheng, X. Cheng, S. J. Choi, A. Chortos, C. Dagdeviren, R. H. Dauskardt, C. A. Di, M. D. Dickey, X. Duan, A. Facchetti, Z. Fan, Y. Fang, J. Feng, X. Feng, H. Gao, W. Gao, X. Gong, C. F. Guo, X. Guo, M. C. Hartel, Z. He, J. S. Ho, Y. Hu, Q. Huang, Y. Huang, F. Huo, M. M. Hussain, A. Javey, U. Jeong, C. Jiang, X. Jiang, J. Kang, D. Karnaushenko, A. Khademhosseini, D. H. Kim, I. D. Kim, D. Kireev, L. Kong, C. Lee, N. E. Lee, P. S. Lee, T. W. Lee, F. Li, J. Li, C. Liang, C. T. Lim, Y. Lin, D. J. Lipomi, J. Liu, K. Liu, N. Liu, R. Liu, Y. Liu, Y. Liu, Z. Liu, Z. Liu, X. J. Loh, N. Lu, Z. Lv, S. Magdassi, G. G. Malliaras, N. Matsuhisa, A. Nathan, S. Niu, J. Pan, C. Pang, Q. Pei, H. Peng, D. Qi, H. Ren, J. A. Rogers, A. Rowe, O. G. Schmidt, T. Sekitani, D. G. Seo, G. Shen, X. Sheng, Q. Shi, T. Someya, Y. Song, E. Stavrinidou, M. Su, X. Sun, K. Takei, X. M. Tao, B. C. K. Tee, A. V. Y. Thean, T. Q. Trung, C. Wan, H. Wang, J. Wang, M. Wang, S. Wang, T. Wang, Z. L. Wang,

P. S. Weiss, H. Wen, S. Xu, T. Xu, H. Yan, X. Yan, H. Yang, L. Yang, S. Yang, L. Yin, C. Yu, G. Yu, J. Yu, S. H. Yu, X. Yu, E. Zamburg, H. Zhang, X. Zhang, X. Zhang, X. Zhang, Y. Zhang, Y. Zhao, S. Zhao, X. Zhao, Y. Zheng, Y. Q. Zheng, Z. Zheng, T. Zhou, B. Zhu, M. Zhu, Y. Zhu, Y. Zhu, G. Zou, X. Chen, Technology roadmap for flexible sensors. *ACS Nano* **17**, 5211–5295 (2023).

51. T. Wang, M. Wang, J. Wang, L. Yang, X. Ren, G. Song, S. Chen, Y. Yuan, R. Liu, L. Pan, Z. Li, W. R. Leow, Y. Luo, S. Ji, Z. Cui, K. He, F. Zhang, F. Lv, Y. Tian, K. Cai, B. Yang, J. Niu, H. Zou, S. Liu, G. Xu, X. Fan, B. Hu, X. J. Loh, L. Wang, X. Chen, A chemically mediated artificial neuron. *Nat. Electron.* **5**, 586–595 (2022).
52. F. Yang, C. Guo, M. Zhang, B. Bhandari, Y. Liu, Improving 3D printing process of lemon juice gel based on fluid flow numerical simulation. *LWT* **102**, 89–99 (2019).
53. A. J. Bandodkar, P. Gutruf, J. Choi, K. Lee, Y. Sekine, J. T. Reeder, W. J. Jeang, A. J. Aranyosi, S. P. Lee, J. B. Model, R. Ghaffari, C. J. Su, J. P. Leshock, T. Ray, A. Verrillo, K. Thomas, V. Krishnamurthi, S. Han, J. Kim, S. Krishnan, T. Hang, J. A. Rogers, Battery-free, skin-interfaced microfluidic/electronic systems for simultaneous electrochemical, colorimetric, and volumetric analysis of sweat. *Sci. Adv.* **5**, eaav3294 (2019).
54. Y. Y. Zhu, X. Zhang, J. Sun, M. Li, Y. Lin, K. Kang, Y. Meng, Z. Feng, J. Wang, A non-enzymatic amperometric glucose sensor based on the use of graphene frameworks-promoted ultrafine platinum nanoparticles. *Microchim. Acta* **186**, 538 (2019).
55. N. Y. Shim, D. A. Bernards, D. J. Macaya, J. A. DeFranco, M. Nikolou, R. M. Owens, G. G. Malliaras, All-plastic electrochemical transistor for glucose sensing using a ferrocene mediator. *Sensors* **9**, 9896–9902 (2009).
56. L. M. Cabello Ballester, I. C. Borrás-Fernández, G. Jovet-Toledo, I. L. Molina-Vicenty, Prevalence of sensory dysfunction in smell and/or taste in veterans with traumatic brain injury and link to demographics and comorbidities. *Mil. Med.* **188**, 555–560 (2023).
57. E. R. Reiter, L. J. DiNardo, R. M. Costanzo, Effects of head injury on olfaction and taste. *Otolaryngol. Clin. North Am.* **37**, 1167–1184 (2004).
58. L. L. Patton, Long-COVID and the practice of oral medicine. *Oral Surg. Oral Med. Oral Pathol. Oral Radiol.* **133**, 125–128 (2022).
59. Y. Dong, S. Chen, T. L. Liu, J. Li, Materials and interface designs of waterproof field-effect transistor arrays for detection of neurological biomarkers. *Small* **18**, e2106866 (2022).
60. T. L. Liu, Y. Dong, S. Chen, J. Zhou, Z. Ma, J. Li, Battery-free, tuning circuit-inspired wireless sensor systems for detection of multiple biomarkers in bodily fluids. *Sci. Adv.* **8**, eabo7049 (2022).
61. J. Chen, S. Tian, X. Wang, Y. Mao, L. Zhao, The Stevens law and the derivation of sensory perception. *J. Future Foods* **1**, 82–87 (2021).
62. C. Yang, Q. Wu, J. Liu, J. Mo, X. Li, C. Yang, Z. Liu, J. Yang, L. Jiang, W. Chen, H. J. Chen, J. Wang, X. Xie, Intelligent wireless theranostic contact lens for electrical sensing and regulation of intraocular pressure. *Nat. Commun.* **13**, 2556 (2022).
63. N. Ranasinghe, E. Y. L. Do, Digital lollipop: Studying electrical stimulation on the human tongue to simulate taste sensations. *ACM Trans. Multimedia Comput. Commun. Appl.* **13**, 1–22 (2016).
64. N. A. Samshir, N. Johari, K. Karunanayaka, A. D. Cheok, Thermal sweet taste machine for multisensory internet, in *Proceedings of the Fourth International Conference on Human Agent Interaction* (Association for Computing Machinery, 2016), pp. 325–328.
65. H. Nakamura, H. Miyashita, Augmented gustation using electricity. In *Proceedings of the Conference on Human Factors in Computing Systems* (Association for Computing Machinery, 2011), pp. 1–2.
66. A. Ullah, Y. Liu, Y. Wang, H. Gao, H. Wang, J. Zhang, G. Li, E-Taste: Taste sensations and flavors based on tongue's electrical and thermal stimulation. *Sensors* **22**, 4976 (2022).
67. Y. Kaji, A. Sato, H. Miyashita, Design of electrical stimulation waveform for enhancing saltiness and experiment on low-sodium dieters. *Front. Virtual Real.* **3**, 879784 (2022).

Acknowledgments: The content was solely the responsibility of the authors and did not necessarily represent the official views of the National Center for Advancing Translational Sciences or the National Institutes of Health. **Funding:** This work was supported by The Ohio State University start-up funds (to J.L.); The Ohio State University Accelerator Award TECG2022-0003 (to J.L.); The National Science Foundation ECCS-2223387 (to J.L.); the National Institute Of Biomedical Imaging And Bioengineering of the National Institutes of Health R21EB035153 (to J.L.); the Defense Advanced Research Projects Agency HR00112410004 (to J.L.); the Chronic Brain Injury Pilot Award Program at The Ohio State University (to J.L.); The Ohio State University Center for Medical and Engineering Innovation pilot grant (to J.L.); The Ohio State University Materials Research Seed Grant Program, funded by the Center for Emergent Materials; NSF-MRSEC, grant DMR-2011876; the Center for Exploration of Novel Complex Materials; the Institute for Materials Research (to J.L.); The Ohio State University Chronic Brain Injury Program 2024 Lannutti Innovation Award (to S.C.); the National Natural Science Foundation of China (grant no. 12072057 and 12472160) (to Z.X.); and Dalian Outstanding Young Talents in Science and Technology (grant no. 2021RJ06) (to Z.X.). **Author contributions:** Conceptualization: S.C., Y.J., P.N., Z.X., and J.L. Methodology: S.C., Y.J., B.D., T.-L.L., P.N., X.T., C.W., and J.L. Investigation: S.C., Y.J., T.-L.L., P.N., and J.L. Visualization: S.C., Y.J., P.N., Z.X., and J.L. Funding acquisition: Z.X. and J.L. Project administration: C.W., Z.X., and J.L. Supervision: Z.X. and J.L. Writing—original draft: S.C., Y.J., B.D., Q.W., C.Y., P.N., Z.X., J.L. Writing—review and editing: S.C., Y.J., Q.W., P.N., X.T., C.Y., C.W., Z.X., J.L. Resources: S.C., Y.J., Z.X., and J.L. Data curation: S.C., Y.J., and J.L. Validation: S.C., Y.J., B.D., X.T., P.N., Z.X., and J.L. Software: Y.J., X.X., X.T., S.C., and Q.W. Formal analysis: S.C., Y.J., and B.D. **Competing interests:** J.L., S.C., Y.J., and T.-L.L. are inventors on a pending provisional patent application (63/656,233) held/submitted by The Ohio State University on 06/05/2024 entitled "Virtual Reality Systems and Methods for Tasting and Taste Sensing". All other authors declare that they have no competing interests. **Data and materials availability:** All data and code needed to evaluate the conclusions in the paper are present in the paper and/or the Supplementary Materials. The code used in this study is publicly available on Zenodo and can be accessed via the 10.5281/zenodo.14503737.

Submitted 2 July 2024
Accepted 27 January 2025
Published 28 February 2025
10.1126/sciadv.adr4797